

# Experimental Fracture Creation in Cores: Permeability and Porosity Measurements of the Fractured Cores and the Use of Such Measurements in Analysis of Pressure Falloff Tests Following Well Stimulation

Mindygaliyeva, B., Uzun, O., Amini, K., Fleckenstein, W. W., and Kazemi, H.  
*Colorado School of Mines, Golden, CO, USA*

Copyright 2023 ARMA, American Rock Mechanics Association

This paper was prepared for presentation at the 57<sup>th</sup> US Rock Mechanics/Geomechanics Symposium held in Atlanta, Georgia, USA, 25-28 June 2023. This paper was selected for presentation at the symposium by an ARMA Technical Program Committee based on a technical and critical review of the paper by a minimum of two technical reviewers. The material, as presented, does not necessarily reflect any position of ARMA, its officers, or members. Electronic reproduction, distribution, or storage of any part of this paper for commercial purposes without the written consent of ARMA is prohibited. Permission to reproduce in print is restricted to an abstract of not more than 200 words; illustrations may not be copied. The abstract must contain conspicuous acknowledgement of where and by whom the paper was presented.

**ABSTRACT:** This paper presents an assessment of the stimulation of an existing, research, geothermal well in a potential enhanced geothermal system (EGS) in Utah, adjacent to the Roosevelt hydrothermal field. The geothermal well has undergone stimulation with the objective to extract heat efficiently from the field's low-permeability granitoid hot rock. This research focuses on deciphering the information content of the stimulated well's pressure transient test using laboratory-measured core data as guides. Specifically, fractures were created in the laboratory in several cores from a non-related granite outcrop and from the Utah FORGE granitoid geothermal reservoir. Matrix and fracture permeabilities and porosities, and pore compressibility were measured and, where appropriate, were used both as guides and input data in the interpretation of the analytical and numerical solutions of flow equations in history matching of the geothermal well measurements. The information obtained from the core experiments was of great value in conventional interpretation of pressure falloff tests. From a pragmatic point of view, our laboratory data suggest that the contribution of the matrix flow to the fracture flow is extremely small, and probably some of the pre-existing natural fractures reopen during well stimulation to provide the main path for fluid flow and, possibly, heat exchange in the stimulated geothermal wells.

## 1. INTRODUCTION

The process of drilling and completion of a pair of parallel injection-production wells in hot, dry rock (HDR) system at 7000-10000 ft depths in the Utah FORGE area is an extensive effort (Moore et al., 2020). Because the permeability and porosity of this HDR system are very small, there is no mobile hot brine in the formation to circulate to sufficiently extract the heat from the formation. The aforementioned injection-production pair shown in Fig. 1 (injector 16A(78)-32 and producer 16B(78)-32) are vertically placed parallel to each other and are intended to be connected by a set of hydraulic fractures (Kumar, D., & Ghassemi, 2019). At this point field attempts have been made to connect the two wells which are 300 ft apart (Allis & Moore, 2019) with three large hydraulic fracture (HF) stages. Each fracture has a relatively large surface area to provide a means of extracting heat from the formation via the injected water flowing through the fracture. However, there is a need for additional surface areas that are perceived as the surface areas of the micro- and macro-fractures in the stimulated volumes between three sets of parallel hydraulic fractures placed in the injection well. One does not know how permeable these smaller fractures are; nonetheless, it is anticipated that some of the innate fractures and the newly

created ones provide additional permeability connection to the HDR matrix (Bruce Hill, 2021).

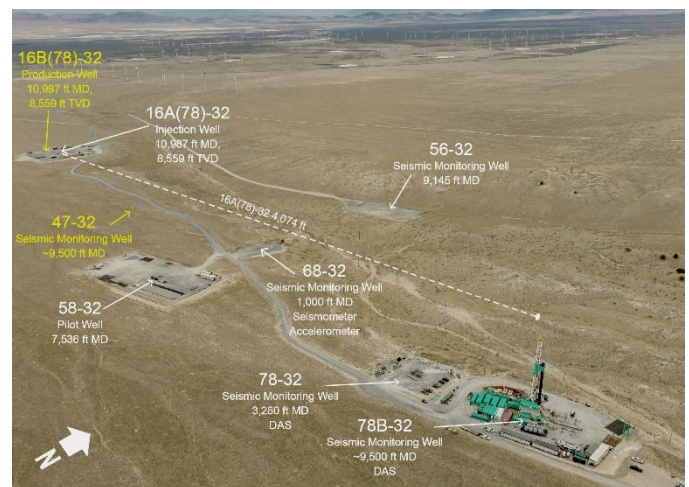


Fig. 1: Northwest aerial view of the Utah FORGE site showing the horizontal component of the trajectory of injector well 16A(78)-32, the surface location of producer well 16B(78)-32, the locations of drill pads for the wells used for tool testing and seismic monitoring (Bruce Hill, 2021).

The geology of south-central Utah is complex and can be characterized by the Quaternary volcanism which explains the anomalously high surface heat flux across the area that has made it an attractive candidate for the

development of geothermal projects (Wells et al., 2022). Another key characteristic of this region is the extensional faulting—Fig. 2a shows the presence of a prominent high-angle fault, called the Opal Mound fault, that dips east creating a hydrological barrier to the lateral flow of the hydrothermal fluids. To the east of this fault, we have the Roosevelt Hot Springs (RHS)—a highly permeable hydrothermal geothermal system. At the RHS the groundwater is predominantly composed of mineralized thermal waters that tend to flow outward to the northwest and west through a shallow unconfined aquifer. The FORGE enhanced geothermal system (EGS) is located 5 km west of RHS shown by the red polygon in Fig. 2a. The basement rocks of the FORGE site are of a crystalline nature composed of the Precambrian gneiss and Tertiary pluton—referred to as granitoid (Nadimi et al., 2020; Simmons et al., 2016). The northwest-southeast cross-section of the FORGE site is shown in Fig. 2b displaying the stratigraphy and isotherms interpreted from well measurements, indicating hotter conditions in the deeper region to the west (Xing et al., 2020).

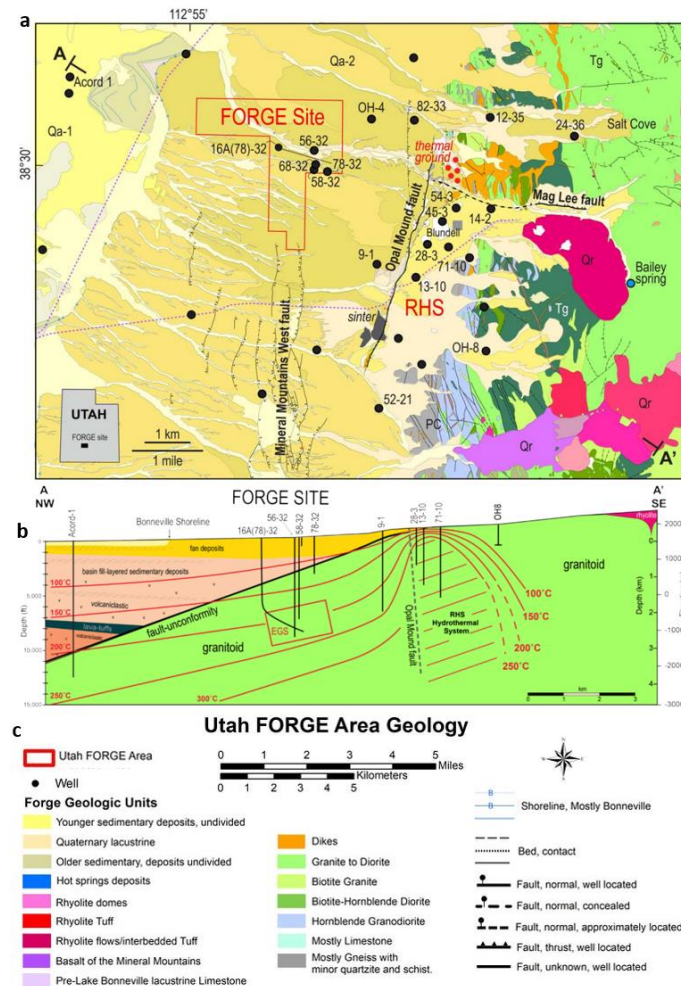


Fig. 2: (a) Geologic map of the FORGE site and surrounding area (Geology, 2022). (b) Geological map: northwest-southeast cross-section of the FORGE Utah site showing the stratigraphy, structure, and thermal regimes (modified from Kirby et al., 2018). (c) FORGE geologic symbols (Geology, 2022).

## 2. EXPERIMENTAL MEASUREMENT TECHNIQUES

The objective of our experiments was to measure the permeability and porosity of the granitoid cores from the FORGE site and an outcrop granite from a non-FORGE site using an automated core measurement instrument (Jones, 1972) before and after fracturing the cores in halves. We obtained the cores' matrix permeability and porosities before and after fracturing. The instrument measures and computes the porosity and permeability of the rock samples at confining stress (or a series of stress steps) of interest within the range of 500-9800 psi. The instrument is programmed to use Boyle's Law to calculate the pore volume (PV) and porosity of samples, capable of providing the measurements for the samples with PV in the range of 0.02–25 cm<sup>3</sup> and permeability in the range of 0.001 micro-Darcy to 5 Darcy. The instrument cannot measure permeability and porosity of an ultra-tight matrix. The confining stress on the cores is achieved by injecting nitrogen gas in a sleeve surrounding the cores under biaxial loading and helium gas is injected into the core for flow measurement at a pressure of 245 psi (Cho, 2012).

First, we conducted experiments on an outcrop granite sample, divided into two core plugs of 1-1/2 inch in diameter by 2 inches in length which met the size requirements for the instrument. The porosity and permeability for one of the core plugs were measured before fracturing. The core was subjected to the net confining stress of 1755 psi and pore pressure of 245 psi. Next, we created a single fracture along the long axis of each core by two methods. The first method involved cutting the granite core sample (designated Granite Core 1, GC1) with a saw as shown in Fig. 3.

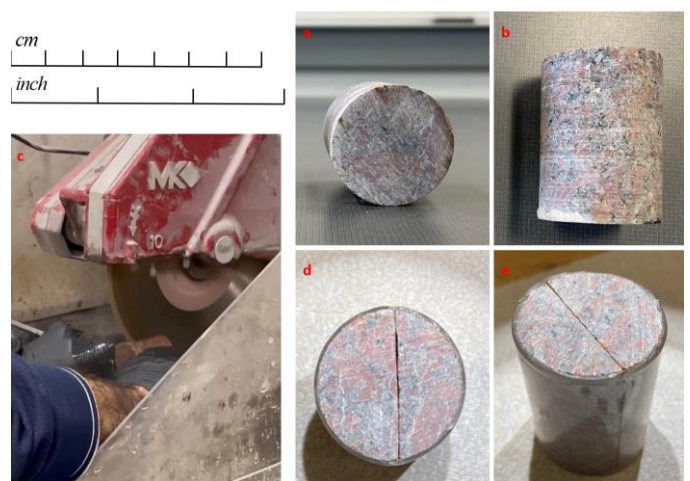


Fig. 3: Granite sample GC1: (a) top view and (b) side view prior to the fracturing (these images are consistent with the scale on the left); (c) cutting core into halves with a saw to create a fracture; (d) top view and (e) side view of the fractured core while wrapped with PVC tape to keep core intact.

In a second method, we used a Material Testing System (MTS) apparatus which creates fracture in the core using an increasing force on the core cylindrical surface. The sample was designated Granite Core 2, GC2, as shown in Fig. 4.

We observed that the fracture that was generated in sample GC2 (Fig. 4: d-e) is a better representative of a nature-like micro-fractures compared to the fracture in sample GC1 (Fig. 3: d-e). In conducting a successful experiment in an automated core measurement apparatus (CMS-300™), we made sure that the core halves remain intact. This was accomplished by wrapping each sample with tape. In the case of sample GC1 (Fig. 3), there was some loss of rock grains in radial direction, therefore, we wrapped it with polyvinyl chloride (PVC) tape to regain the correct diameter dimension necessary for the apparatus. There were no issues with the post-frac diameter of sample GC2 (Fig. 4); however, Teflon tape was used to keep the core halves together. The porosity and permeability of the fractured cores were measured under the identical confining stress of 1755 psi and 245 psi of pore pressure.



Fig. 4: Granite sample GC2: (a) top view and (b) side view prior to fracturing (these images are consistent with the scale on the left); (c) the sample and MTS machine to create a fracture; (d) top view and (e) side view of the fractured core while the core is wrapped with Teflon tape to keep core intact.

The fracturing procedures depicted in Fig. 3 and 4 were applied to two granitoid cores which were retrieved from the Utah FORGE injector well 16A(78)-32. The horizontal core A4-9H, Fig. 5b, is from the measured depth (MD) of 10981.9 ft, and the vertical core A3-8V, Fig. 6b, is from the measured depth of 10955.9 ft. The permeability and porosity of horizontal core A4-9H were measured before fracturing by our core measurement apparatus at net confining stresses 1255 psi, 1755 psi, and 2755 psi and pore pressure of 245 psi. The apparatus could not provide the measurements for the vertical core A3-8V under the net confining stress of 2755 psi, thus the flow properties for the core before fracturing were

measured at net confining stresses 1255 psi, 1555 psi, 1755 psi, and 2255 psi. The measurements were also repeated for these granitoid cores in the reverse order. Afterward, the core A4-9H (Fig. 5b) was successfully cut with a saw and permeability measurements were conducted as indicated earlier.

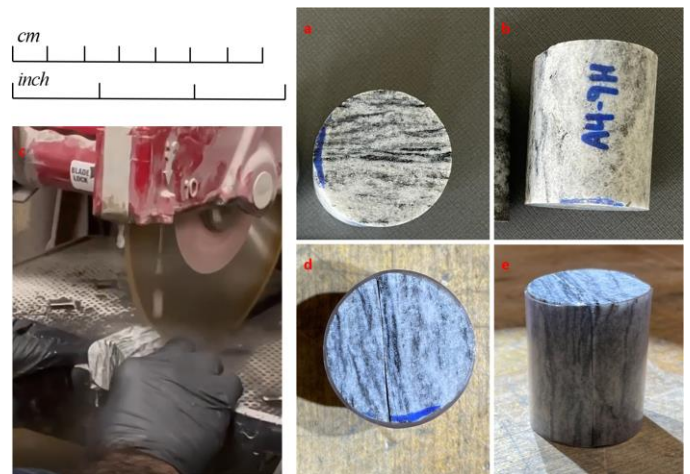


Fig. 5: FORGE horizontal core A4-9H: (a) top view and (b) side view prior to fracturing (these images are consistent with the scale on the left); (c) cutting core into halves with a saw to create a fracture; (d) top view and (e) side view of the fractured core while wrapped with PVC tape to keep core intact.

In generating fracture in vertical core, A3-8V, in Fig. 6b, with the MTS machine, under an applied controlled force rate, the core crumbled which prevented creating a fracture (Fig. 6d)!

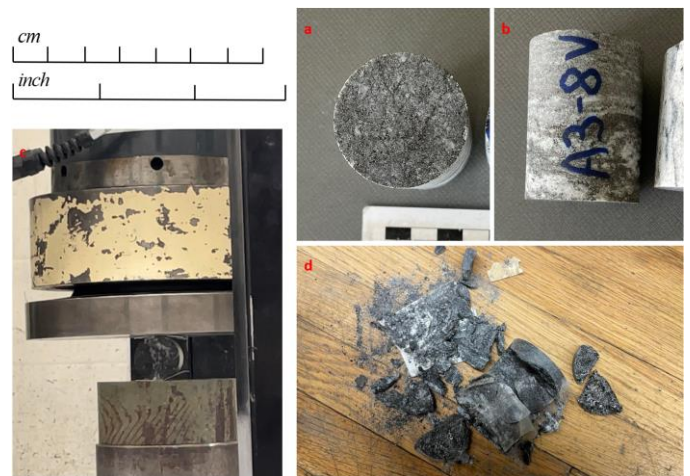


Fig. 6: FORGE vertical sample A3-8V: (a) top view and (b) side view prior to fracturing (these images are consistent with the scale on the left); (c) the sample and MTS machine to create a fracture; (d) failure to generate fracture due to crumbling.

In spite of experimental issues, we were able to obtain viable measured results from the core experiments to be used as input data into our mathematical modeling and analysis of the Utah FORGE pressure falloff tests.

### 3. ANALYSIS OF EXPERIMENTAL RESULTS

We conducted laboratory core measurements with automated core measurement apparatus before and after fracture for the two outcrop granite cores, GC1 and GC2 (Fig. 3-4, Table 1), and for the FORGE horizontal granitoid core, A4-9H (Fig. 5b, Table 2). For the FORGE vertical granitoid core, A3-V (Fig. 6b, Table 3), we ran experiments before the fracture only, since the sample crumbled. The results obtained from the experimental runs are included in this section. A schematic of a core sample post-fracture is illustrated below, where Fig. 7a depicts a more realistic representation while Fig. 7b is an idealized version of the fractured core assuming the fracture is uniform and has no roughness. Thus, in Fig. 7c we illustrate that such an assumption simplifies the task of fracture aperture (width) calculation by allowing us to express the total surface area of the top of the fractured core in terms of the surface area of the rock matrix ( $A_m$ ) and the surface area of the fracture ( $A_f$ ), see Eq. (1) – (6).

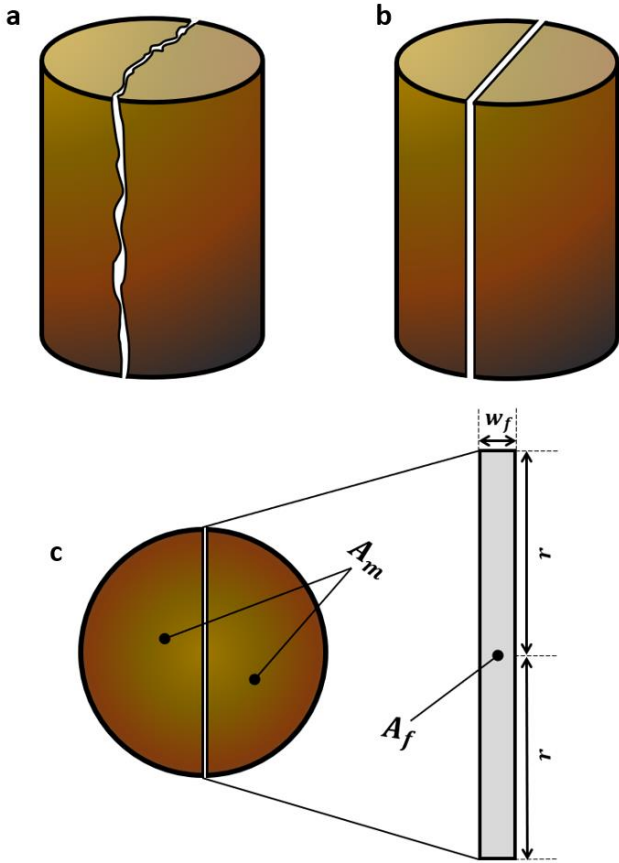


Fig. 7: (a) Schematic of the core post-fracture used in apparatus measurements; (b) idealized schematic of the core post-fracture; and (c) top view of idealized schematic illustrating surface areas of the matrix and fracture (and its aperture).

$$A_t = A_m + A_f = \pi r^2 = \frac{\pi d^2}{4} \quad (1)$$

$$A_f = 2rw_f = dw_f \quad (2)$$

$$\phi_f = \frac{A_f}{A_t} = \frac{2rw_f}{\pi r^2} = \frac{dw_f}{\frac{\pi d^2}{4}} = \frac{4}{\pi d} w_f \quad (3)$$

$$k_f = 10^3 \frac{w_f^2}{12} \quad (4)$$

$$k_{f,eff} = k_f \phi_f + k_m = \left( \frac{10^3}{3\pi d} \right) w_f^3 + k_m \quad (5)$$

$$w_f = \sqrt[3]{0.003\pi d(k_{f,eff} - k_m)} \quad (6)$$

The tabulated results illustrate the significant difference in the permeability of the cores before and after the presence of the fracture. Thus, in a formation, presence of an open conductive fracture, reopening of a closed fracture, or creation of a new fracture that is connected to a hydraulic fracture would greatly improve the ability of fluids to flow within the fracture, and would provide more surface area of the rock for a potential circulating fluid in a geothermal system to extract or transport thermal energy. An important physical property of a fractured rock is its effective permeability ( $k_{f,eff} = k_f \phi_f + k_m$ ) which is generally much larger than the surrounding matrix permeability. This would allow fluids such as water to flow easily through the fracture when pressure or gravity gradient is imposed on the fluid.

Table 1: Experimental results for Granite Cores (Fig. 3-4) under net confining stress of 1755 psi and pore pressure of 245 psi.

| Core | Description                 | $\phi, \%$      | $k, \text{mD}$               |
|------|-----------------------------|-----------------|------------------------------|
| GC2  | before fracturing           | $\phi_m = 0.99$ | $k_m = 3.68\text{E-}4$       |
| GC2  | after fracturing with MTS   | $\phi_t = 2.07$ | $k_{f,eff} = 4.16\text{E+}2$ |
| GC1  | after fracturing with a saw | $\phi_t = 1.18$ | $k_{f,eff} = 8.16\text{E+}2$ |

Table 2: Porosity and permeability for FORGE horizontal core A4-9H (Fig. 5b) before and after fracturing.

| Data Before Fracturing |              |                        |
|------------------------|--------------|------------------------|
| $\sigma_c, \text{psi}$ | $\phi_m, \%$ | $k_m, \text{mD}$       |
| 1255                   | 0.73         | 1.09E-2                |
| 1755                   | 0.73         | 7.70E-3                |
| 2755                   | 0.65         | 2.73E-3                |
| 2755                   | 0.61         | 2.65E-3                |
| 1755                   | 0.70         | 3.68E-3                |
| 1255                   | 0.76         | 7.22E-3                |
| Data After Fracturing  |              |                        |
| $\sigma_c, \text{psi}$ | $\phi_t, \%$ | $k_{f,eff}, \text{mD}$ |
| 1255                   | 1.41         | 4.39E+3                |
| 1755                   | 1.33         | 4.89E+3                |
| 2755                   | 1.22         | 3.61E+3                |
| 2755                   | 1.20         | 3.62E+3                |
| 1755                   | 1.26         | 4.39E+3                |
| 1255                   | 1.30         | 4.82E+3                |

Table 3: Porosity and permeability for FORGE vertical core A3-8V (Fig. 6b) before crumbling.

| Data Before Crumbling |              |            |
|-----------------------|--------------|------------|
| $\sigma_c$ , psi      | $\phi_m$ , % | $k_m$ , mD |
| 1255                  | 0.44         | 3.16E-4    |
| 1555                  | 0.40         | 2.42E-4    |
| 1755                  | 0.31         | 2.35E-4    |
| 2255                  | 0.04         | 1.74E-4    |
| 2255                  | 0.11         | 1.78E-4    |
| 1755                  | 0.12         | 1.97E-4    |
| 1555                  | 0.22         | 2.28E-4    |
| 1255                  | 0.27         | 2.45E-4    |

Additionally, we can observe that our samples have low porosities, even after fracture creation. A reservoir with very low porosity would indicate that the rock in the reservoir has a very low capacity to hold fluids, such as water. Porosity is the measure of the volume of the void spaces, or pores, in a rock formation, and it is a critical parameter in determining the amount of fluid that can be stored in a reservoir, if any. To develop a low porosity geothermal reservoir, specialized drilling and completion techniques may be required to maximize the connectivity between the wellbore and the available pore space in the rock.

Granitoids that are formed at great depths in the Earth's crust can be subject to high temperature and pressure conditions. These conditions can cause the minerals within the rock to become more tightly packed, reducing the amount of pore space available for fluids, thus reducing the permeability. The slow cooling rates of deep granitoids can also contribute to their low porosity and permeability. As the magma cools, the minerals have more time to crystallize and grow, filling in any available pore space. The tectonic stresses that can occur at great depths can cause the minerals within granitoids to become more tightly packed, reducing the amount of pore space available for fluids and its ability to flow. The chemical alteration of granitoids over time can also lead to reduced porosity and permeability. For example, minerals such as feldspar can undergo hydrothermal alteration and become more compact, further reducing the amount of pore space available (Brown, 2013; Frost et al., 2001). Overall, deep granitoids can have ultra-low porosity due to a combination of factors related to their formation, cooling, and subsequent geological processes. This can make it more challenging to produce geothermal energy from these reservoirs but advances in drilling and stimulation technologies may make it possible to unlock their potential in the future. Enhanced geothermal systems (EGS) technologies, such as hydraulic fracturing or other stimulation methods, may also be used to increase the permeability of the reservoir and improve fluid flow which in return will yield a better thermal energy recovery.

#### 4. INCORPORATING LABORATORY-MEASURED DATA IN PRESSURE TRANSIENT ANALYSIS OF FIELD DATA

This section presents an analysis of the pressure falloff in the open-hole section of FORGE injection well 16A(78)-32. Specifically, the test is from Stage 1 HF which was conducted in April of 2022. The objective of the analysis is to decipher the information content of the test—a variant of the classic diagnostic fracture injection test (DFIT). The test contains valuable information about the effectiveness of the stimulation in the drainage volume of Well 16A(78)-32. Stage 1 HF was conducted in the open hole section, 10826 ft to 10828 ft MD, or 8512 ft TVD, using slickwater fracturing fluid (Fig. 8). The total volume of pumped slickwater was 4327 bbl. The rudiments of the analysis we conducted is embedded in the classic pressure transient analysis (PTA) in petroleum reservoirs. The superposition of single-rate solution for linear flow regime was applied to our multi-rate data. The analysis yielded an effective permeability in the stimulated volume two orders of magnitude larger than matrix permeability from cores. The measured permeability of the fractured cores is the effective permeability of the fracture cut in core plus matrix permeability. This information is extrapolated, via numerical modeling and history matching, to the stimulated volume of the Stage 1 HF in Well 16A(78)-32 (Kurtoglu et al., 2012).

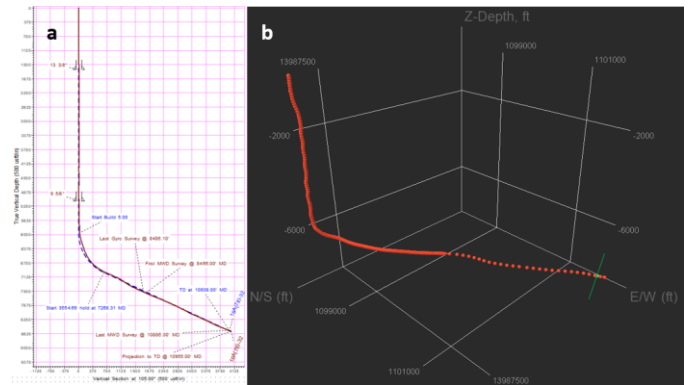


Fig. 8: (a) Directional profile showing approximate elevation view (Winkler et al., 2021); (b) plotted deviation survey in Spotfire where green line illustrates the spatial location of the Stage 1 HF.

The process of water circulation through a fracture network system is complex (Fig. 9), as it depends on several factors such as the geometry and connectivity of the fractures, the hydraulic conductivity of the rock, and the pressure and temperature gradients within the system. In an EGS, cold water is injected into the underground reservoir through an injection well. As the injected water flows through the rock, it encounters fractures and other permeable structures that provide pathways for the water to flow through (Fig. 9a). As the water flows through the fractures, it interacts with the surrounding rock,

exchanging heat and solutes with the rock matrix (Fig. 9b). After the heated water has circulated through the

reservoir, it is then extracted through a production well (Fig. 9c).

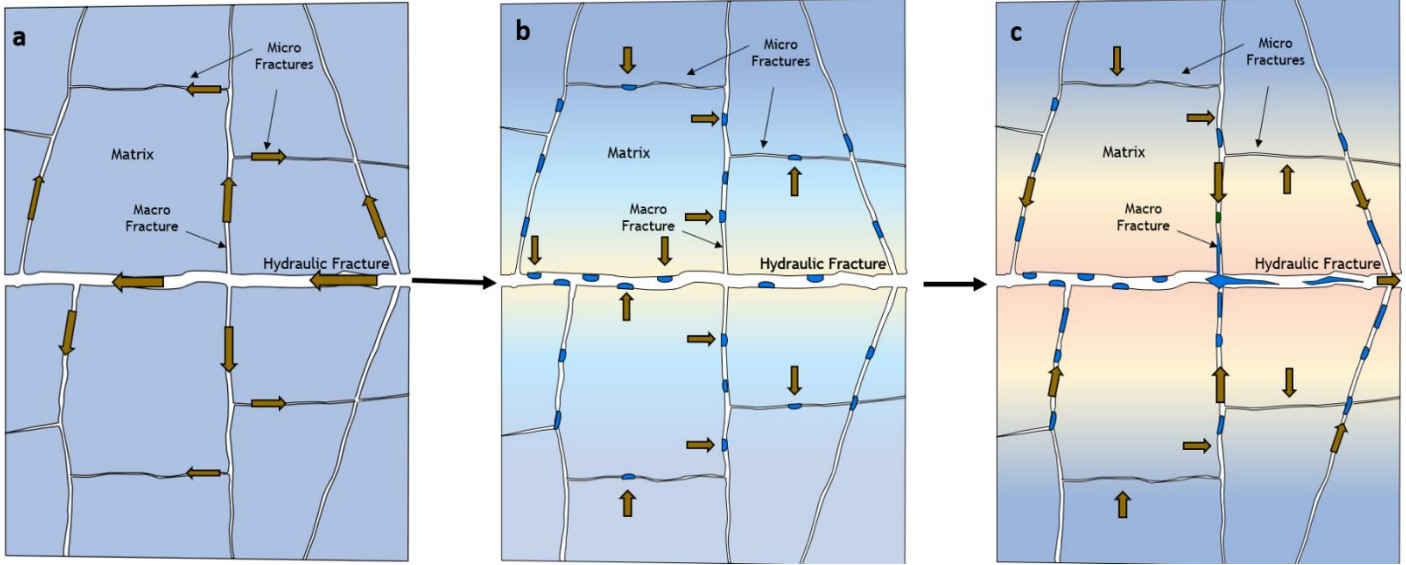


Fig. 9. (a) Existing and induced fracture network; (b) water flows through stimulated micro- and macro-fractures to reach matrix; (c) water flows to the wellbore.

Deciphering the pressure transient behavior of horizontally fractured wells in tight, fractured formations is crucial for two main reasons. Firstly, the interpretation of pressure transient responses is complicated by the complex interaction between horizontal well, hydraulic fracture, natural fractures, and tight matrix. (Medeiros et al., 2007). Secondly, the production of long, hydraulically fractured horizontal wells in tight formations is driven by unsteady-state transient flow regimes for extended periods of time (Medeiros et al., 2008).

The field pressure and flow rate data during Stage 1 HF treatment are shown in Fig 10. The bottomhole treating pressure, in psi, was calculated by adding the hydrostatic head of treating fluid to the surface pressure without including any friction losses (because the injected fluid is slickwater—a friction reducing polymer, and during pressure falloff period the injection rate is zero; thus, no friction loss in the wellbore). The calculated bottomhole pressure data are plotted in red, and the slickwater rate in bpm in blue.

We analyzed the pressure falloff behavior to determine the flow characteristics of this geothermal reservoir and well, such as the effective formation permeability ( $k_{f,eff}$ ) and its relationship to stimulated micro- and macro-fractures in the stimulated volume.

The pressure falloff equation for multi-rate in a hydraulic fracture is:

$$p_i - p_{ws}(t_N + \Delta t) = \frac{4.064 q_N \mu}{\sqrt{k_{f,eff}(hL_f)}} \left( \frac{1}{(\phi c_t)_{f+m} \mu} \right)^{\frac{1}{2}} \times \left[ \sum_{j=1}^N \frac{q_j}{q_N} (\sqrt{(t_N + \Delta t) - t_{j-1}} - \sqrt{(t_N + \Delta t) - t_j}) \right] \quad (7)$$

Rearranging Eq. (7) we obtain:

$$p_{ws}(t_N + \Delta t) = p_i - \frac{4.064 q_N \mu}{\sqrt{k_{f,eff}(hL_f)}} \left( \frac{1}{(\phi c_t)_{f+m} \mu} \right)^{\frac{1}{2}} \times \left[ \sum_{j=1}^N \frac{q_j}{q_N} (\sqrt{(t_N + \Delta t) - t_{j-1}} - \sqrt{(t_N + \Delta t) - t_j}) \right] \quad (8)$$

The coefficient in front of the bracketed term in Eq. (8) represents the absolute value of the slope of the straight-line segment as shown by Eq. (9):

$$m = \frac{4.064 q_N \mu}{\sqrt{k_{f,eff}(hL_f)}} \left( \frac{1}{(\phi c_t)_{f+m} \mu} \right)^{\frac{1}{2}} \quad (9)$$

Rearranging Eq. (9) we obtain fracture system effective permeability Eq. (10):

$$k_{f,eff} = \left( \frac{4.064 q_N \mu}{m(hL_f)} \right)^2 \left( \frac{1}{(\phi c_t)_{f+m} \mu} \right) \quad (10)$$

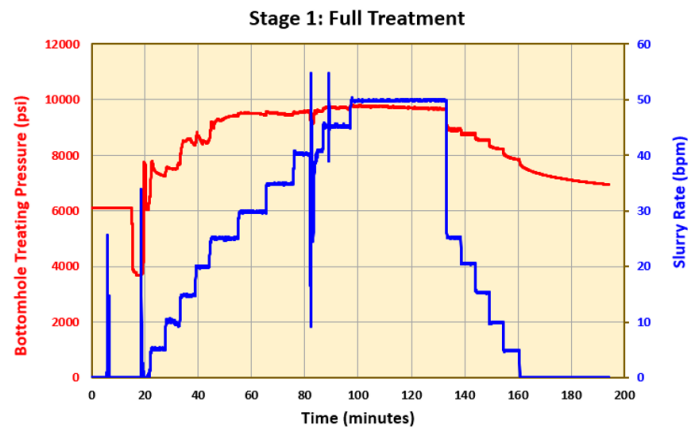


Fig. 10: Stage 1 treatment data in FORGE Well 16A(78)-32. Bottomhole treating pressure is shown in red (psi) and slickwater rate is shown in blue (bpm).

Table 4: Tabulated multistep flow rate data for Stage 1 HF completed in FORGE Well 16A(78)-32.

| Designation | Time, min | Flow Rate, bbl/min | Time, hour | Flow Rate, bbl/day |
|-------------|-----------|--------------------|------------|--------------------|
| $q_1$       | 78.47     | 49.85              | 1.31       | 71784.0            |
| $q_2$       | 83.94     | 25.46              | 1.40       | 36662.4            |
| $q_3$       | 89.25     | 20.50              | 1.49       | 29520.0            |
| $q_4$       | 94.59     | 15.36              | 1.58       | 22118.4            |
| $q_5$       | 99.94     | 9.940              | 1.67       | 14313.6            |
| $q_6$       | 106.04    | 4.910              | 1.77       | 7070.40            |

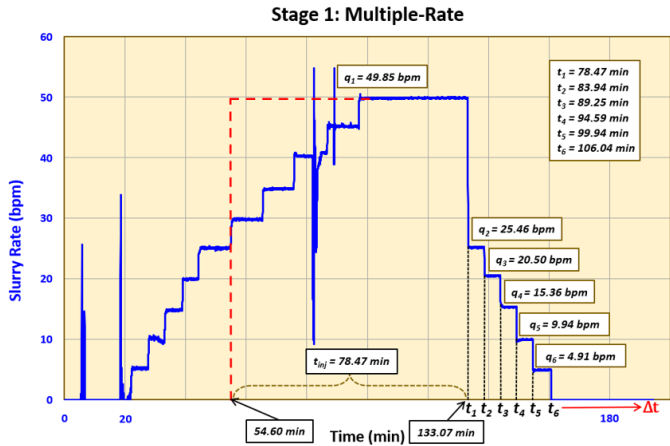


Fig. 11: Data from Table 4 is plotted on top of the actual data for application of superposition Eq. (7) for variable flow rate.

## 5. RESULTS

To identify the straight-line segment on the field data we plotted  $p_{ws}(t_N + \Delta t)$  vs.  $\sum_{j=1}^N \frac{q_j}{q_N} (\sqrt{(t_N + \Delta t) - t_{j-1}} - \sqrt{(t_N + \Delta t) - t_j})$  as shown in Fig. 12. The absolute value of the slope ( $m$ ) of the straight-line segment equals 278.95 and its physical meaning is mathematically represented by Eq. (9).

By finding the straight-line intercept at  $\Delta t \rightarrow \infty$ , we obtained an estimate of initial formation pressure of 5264 psi as shown in Fig. 13 assuming there is some sort of fluid, such as gas, in the formation pores. At  $\Delta t = 0$  on the straight-line segment, the apparent pressure drop due to skin is represented by the difference between pressure on the straight-line segment and the initial shut-in pressure on the pressure falloff curve ( $\Delta p_{skin} = 280$  psi). We used the above pressure drop to estimate the skin factor:  $\Delta p_{skin} = \frac{141.2q_N \mu}{kh} s_{hf}^{face}$ , yielding  $s_{hf}^{face} = 0.596$ . This positive skin factor is caused by both fracture closing and, perhaps, reflecting the presence of the higher viscosity filtrate in the invasion zone adjacent to the fracture face compared with the viscosity of the resident fluid (gas) beyond the filtrate zone.

Before we had core experimental measurements, we relied on the flow properties obtained from the literature review shown in Table 5. With these parameters the calculated effective formation permeability ( $k_{f,eff}$ ) was 0.492 mD. Table 6 outlines the results of the initial analytical analysis of the field pressure falloff data.

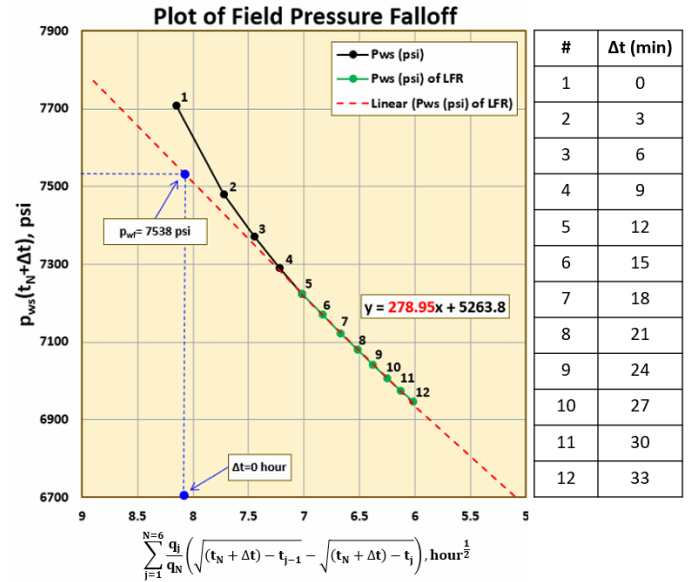


Fig. 12: Plot of shut-in bottomhole field pressure data (y-axis) versus the time summation (x-axis).

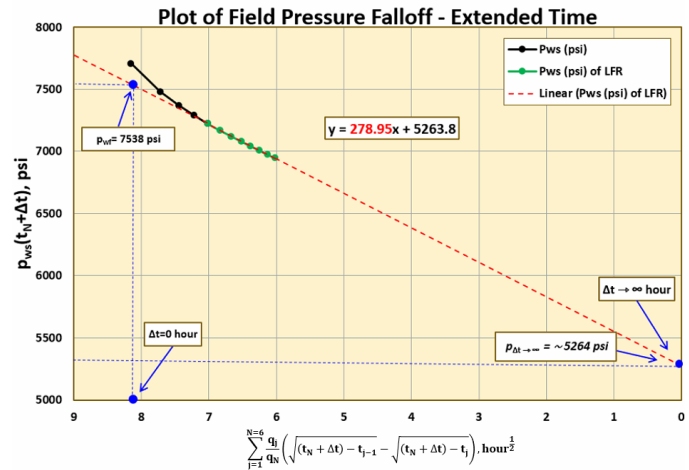


Fig. 13: Extended plot of shut-in bottomhole field pressure data (y-axis) versus the time summation (x-axis) to obtain the straight-line intercept for the estimate of the initial reservoir pressure.

We decided to focus on the experimental results for the FORGE Core A4-9H under the net confining pressure of 2755 psi (see Table 2 or Table 8) to compute the fracture aperture ( $w_f$ ), experimentally created in the core, by using Eq. (6). The calculated fracture width equals  $108 \mu m$ . Then we recalculated the effective formation permeability ( $k_{f,eff}$ , refer to Table 7) using the slope obtained from the analytical analysis of the field data for the different cases of matrix block dimensions ( $L_x=L_y=L_z$ ) by using fracture

width ( $w_f=108 \mu\text{m}$ ) and fracture porosity ( $\phi_f$ , refer to Table 7) determined with Eq. (11).

$$\phi_f = \frac{w_f(L_x+L_y)}{2L_xL_y} \quad (11)$$

Table 5: Data utilized in the initial analytical analysis of the pressure falloff data independent of laboratory experiments where (a) represents near equilibrium temperature at the reservoir depth (Allis, R. et al., 2018), (b) is water viscosity at 358°F (181°C), (c) fracture height of 200 m ( $h=2L_f$ , Nadimi et al., 2020), and (d) porosity obtained from the data shared in the FORGE project's numerical modeling forum (Utah FORGE, 2019).

| Parameter    | Unit                  | Value              |
|--------------|-----------------------|--------------------|
| $T^{(a)}$    | °F (°C)               | 358 (181)          |
| $q$          | RB/D                  | 7070.4             |
| $\mu^{(b)}$  | cP                    | 0.152              |
| $h^{(c)}$    | ft (m)                | 656 (200)          |
| $L_f^{(c)}$  | ft (m)                | 328 (100)          |
| $\phi^{(d)}$ | –                     | 0.0118             |
| $c_i$        | psi <sup>-1</sup>     | $6 \times 10^{-6}$ |
| $m$          | psi/hr <sup>1/2</sup> | 278.95             |

Table 6: Results of the pressure transient analysis of the field falloff test data using input parameters shared in Table 5.

| Results (a) – Analytical Analysis                                                      |                                |       |
|----------------------------------------------------------------------------------------|--------------------------------|-------|
| Results of analytical PTA of field pressure falloff data using inputs shown in Table 5 | $P_{\text{reservoir}}$ , psi   | 5264  |
|                                                                                        | $\Delta p_{\text{skin}}$ , psi | 280   |
|                                                                                        | $S_{hf}^{\text{face}}$         | 0.596 |
|                                                                                        | $k_{f,eff}$ , mD               | 0.492 |

## 6. MATHEMATICAL MODELING

Next, we generated a 1-dimensional (1D) dual-porosity model (Alruwayi et al., 2021; Eker et al., 2017) with several matrix block geometries in order to de-convolve the fracture-matrix transport effects as guided by well pressure measurement and laboratory core experimental results (FORGE horizontal core A4-9H, in Fig. 5b, under the net confining pressure of 2755 psi and 245 psi of pore pressure, refer to Table 2 and Table 8). The computer code for this model is an in-house document.

We modeled two scenarios: one with matrix block sizes of 5 ft × 5 ft (Fig. 14) and a second with matrix block sizes of 1 ft × 1 ft (Fig. 15). The slopes and effective formation permeabilities ( $k_{f,eff}$ ) obtained from the analysis of the numerical outputs are in strong agreement with the analytical solution analysis of the field pressure falloff data. These independent mathematical approaches provide credence to the potential viability of our analysis.

Table 7: Updated effective formation permeability values attained by using the slope obtained from PTA of the field pressure falloff data for different matrix block dimensions.

| Results (b) – Analytical Analysis |                         |                  |
|-----------------------------------|-------------------------|------------------|
| Case                              | $\phi_f$                | $k_{f,eff}$ , mD |
| $L_{x,y,z} = 5 \text{ ft}$        | $7.0807 \times 10^{-5}$ | 0.884            |
| $L_{x,y,z} = 1 \text{ ft}$        | $3.5403 \times 10^{-4}$ | 0.847            |

Table 8: Input data used in 1D dual-porosity model for the two cases (Fig. 14 and Fig. 15) and results associated with the numerically generated pressure falloff curves.

| Input Data Case 1 in Fig. 14 |                         | Input Data Case 2 in Fig. 15 |                         |
|------------------------------|-------------------------|------------------------------|-------------------------|
| $L_{x,y,z}$ , ft             | 5                       | $L_{x,y,z}$ , ft             | 1                       |
| $\phi_m$                     | 0.0065                  | $\phi_m$                     | 0.0065                  |
| $\phi_f$                     | $7.0807 \times 10^{-5}$ | $\phi_f$                     | $3.5403 \times 10^{-4}$ |
| $k_m$ , mD                   | 0.00273                 | $k_m$ , mD                   | 0.00273                 |
| $k_{f,eff}$ , mD             | 0.884                   | $k_{f,eff}$ , mD             | 0.847                   |
| Results (c) Case in Fig. 14  |                         | Results (d) Case in Fig. 15  |                         |
| $m$ , psi/hr <sup>1/2</sup>  | 275.22                  | $m$ , psi/hr <sup>1/2</sup>  | 278.81                  |
| $k_{f,eff}$ , mD             | 0.908                   | $k_{f,eff}$ , mD             | 0.848                   |

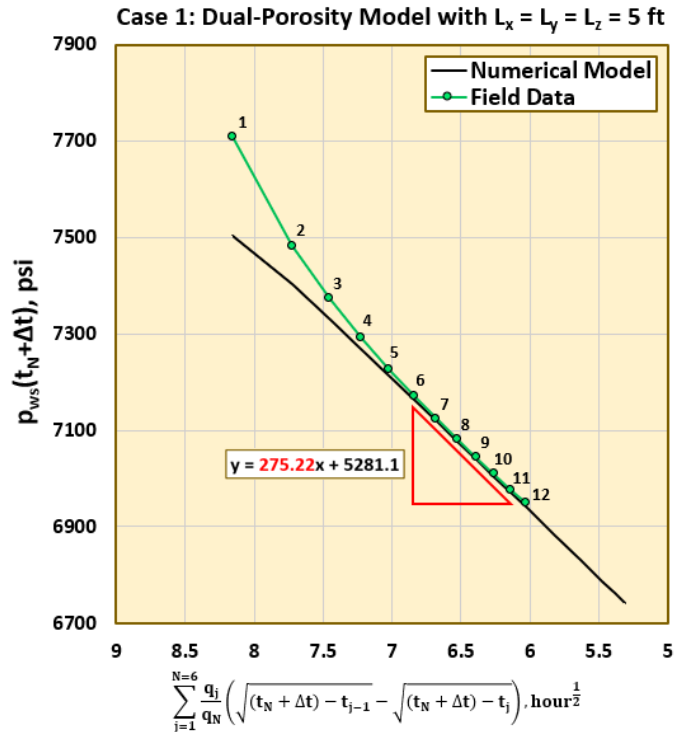


Fig. 14: Plot of numerical pressure falloff in black and field pressure falloff in green (y-axis) versus the time summation (x-axis). We used 1D dual-porosity numerical model with matrix block size of 5-by-5 ft and input parameters from Table 2 for  $\sigma_c=2755 \text{ psi}$  (also see Table 8).

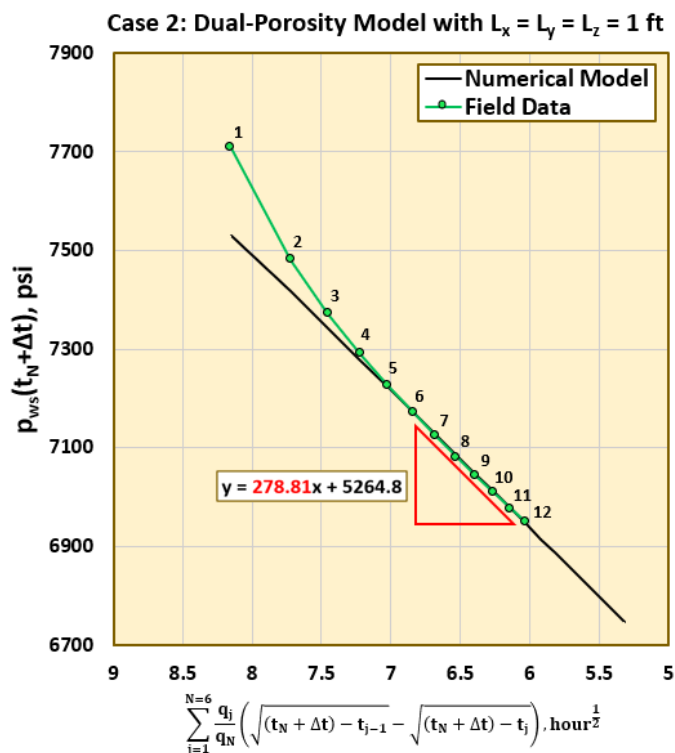


Fig. 15: Plot of numerical pressure falloff in black and field pressure falloff in green (y-axis) versus the time summation (x-axis). We used 1D dual-porosity numerical model with matrix block size of 1-by-1 ft and input parameters from Table 2 for  $\sigma_c = 2755$  psi (also see Table 8).

The fracture permeability values, calculated from pressure falloff analysis and numerical modeling, are highly dependent on matrix block dimensions, which we consider a statistical measure of the fracture spacings of conductive fractures. Using the effective fracture permeability calculated from the field data in Fig. 14 and assuming matrix block size of 5 feet, we obtained fracture intrinsic permeability of 12500 mD. Similarly using the effective fracture permeability calculated from the field data in Fig. 15 and assuming a matrix block size of 1 foot, we obtained fracture intrinsic permeability of 2400 mD. Thus, if we assume that fracture spacing of 5 feet is more representative of the stimulated FORGE environment, then the micro-fractures have a permeability of about 12500-13000 mD.

Another significant uncertainty in calculating the stimulated formation permeability is the hydraulic fracture height which we used 656 feet. If we use 328 feet for the fracture height, the calculated effective fracture permeability increases by a factor of 4 (that is, 3.534 MD compared to 0.884 mD). This uncertainty will be minimized if the length and the height of the hydraulic fracture are ascertained via appropriate field measurements (such as microseismic).

## 7. DISCUSSION

The laboratory core measurements provided porosity and permeability of unfractured and fractured outcrop granite and FORGE granitoid cores (Tables 1, 2 and 3). All cores have very low matrix permeabilities ( $\sim 0.001$ ) and very low porosities ( $\sim 0.005$ ). Any differences in the properties for these rocks are due to the nature of their geologic settings. For instance, the outcrop granite core sample came from an exposed surface; therefore, it has been subjected to atmospheric weathering. While the granitoid cores were obtained from a very deep location: therefore, they were subjected to very high stress and temperature.

In comparing the granitoid matrix permeability (Table 2-3) to the effective formation permeability,  $k_{f,eff}$ , obtained from the PTA analysis of the pressure falloff data (Table 6 and 8) we observe a substantial difference. Specifically, the PTA yielded  $k_{f,eff}$  two to three orders of magnitude larger than the matrix permeability of the granitoid. This clearly is an indication of the presence of permeable macro-fractures and micro-fractures resulting from generation of fractures and/or reopening of previous fractures. We also conducted a wettability experiment on a FORGE core (A4-9H, Fig 5b) which indicated a water-wet behavior; thus, capable of imbibing injected water. This potentially would provide a measure of quantity of water that could enter the tight matrix, essentially, as an immobile phase.

## 8. CONCLUSIONS

1. We have presented analytical and numerical analyses of the pressure falloff data of Stage 1 HF of FORGE injection well 16(A)78-32. The analyses clearly indicate the presence of highly conductive micro- and macro-fractures associated with a Satge 1 HF.
2. We used outcrop granite and FORGE granitoid core samples to obtain key flow properties (permeability and porosity) of micro-fractured rocks associated with the downhole environment (Tables 1, 2, and 3).
3. We used the laboratory measured properties of outcrop granite and FORGE granitoid rock samples in the analyses of the shut-in pressure tests to infer information about the stimulated FORGE environment.
4. The fracture permeability values, calculated from pressure falloff analysis and numerical modeling, are highly dependent on matrix block dimensions, which we consider a statistical measure of the fracture spacings of conductive fractures. From the analyses of field data, via analytical and numerical modeling, we conclude that the intrinsic stimulated fracture permeabilities are on the order of  $10^3$  to  $10^4$  mD.

- Employing reservoir engineering methods, such as the techniques we used in the pressure falloff analysis and numerical modeling, it is also possible to improve the efficiency of heat extraction from the reservoir.

## ACKNOWLEDGMENTS

First, we acknowledge great support from Mr. Jim Wendy Marquardt, owner at Terra mechanics LLC, and Professor John McLennan at The University of Utah for providing Utah FORGE core samples. Second, this material is based upon work supported by the Department of Energy, Office of Energy Efficiency and Renewable Energy (EERE), under Award Number DE-EE0007080. This report was prepared as an account of work sponsored by an agency of the United States Government. Neither the United States Government nor any agency thereof, nor any of their employees, makes any warranty, express or implied, or assumes any legal liability or responsibility for the accuracy, completeness, or usefulness of any information, apparatus, product, or process disclosed, or represents that its use would not infringe privately owned rights. Reference herein to any specific commercial product, process, or service by trade name, trademark, manufacturer, or otherwise does not necessarily constitute or imply its endorsement, recommendation, or favoring by the United States Government or any agency thereof. The views and opinions of authors expressed herein do not necessarily state or reflect those of the United States Government or any agency thereof.

## NOMENCLATURE

$\mu$  = Slickwater viscosity, cP  
 $\phi_t$  = Total porosity  
 $\phi_f$  = Fracture porosity  
 $\phi_m$  = Matrix porosity  
 $A_t$  = Top circular surface area of cylinder,  $\mu\text{m}^2$   
 $A_f$  = Surface area of fracture in the cylinder top,  $\mu\text{m}^2$   
 $A_m$  = Surface area of matrix in the cylinder top,  $\mu\text{m}^2$   
 $c_t$  = Total compressibility,  $\text{psi}^{-1}$   
 $d$  = Core sample diameter,  $\mu\text{m}$   
 $h$  = Formation thickness, ft  
 $j$  = Number of rate steps: 1, 2, ..., N  
 $k_f$  = Fracture permeability, mD  
 $k_{f,eff}$  = Effective formation permeability, mD  
 $k_m$  = Matrix permeability, mD  
 $L_x$  = Matrix block side length in the x-direction, ft  
 $L_y$  = Matrix block side length in the y-direction, ft  
 $L_z$  = Matrix block side length in the z-direction, ft  
 $L_f$  = Fracture half-length, ft  
 $m$  = Slope of the straight-line segment

$p_i$  = Initial pressure, psi  
 $p_{ws}$  = Shut-in bottomhole pressure, psi  
 $q_j$  = Rate at step number  $j$ , bpd  
 $q_N$  = Final rate before shut-in, bpd  
 $t_N$  = Starting time of shut-in period, hr  
 $\Delta t$  = Shut-in time, hr  
 $w_f$  = Fracture width or aperture,  $\mu\text{m}$

## REFERENCES

- Allis, R., Gwynn, M., Hardwick, C., & Moore, J. (2018). The challenge of correcting bottom-hole temperatures – An example from FORGE 58-32, near Milford, Utah. *Proceedings, 43rd Workshop on Geothermal Reservoir Engineering, Stanford University, Stanford, CA.*
- Allis, R., & Moore, J. N. (2019). *Geothermal Characteristics of the Roosevelt Hot Springs System and Adjacent FORGE EGS Site, Milford, Utah: Utah Geological Survey Miscellaneous Publication 169, IX.* <https://doi.org/https://doi.org/10.34191/MP>
- Alruwayi, S. A., Uzun, O., & Kazemi, H. (2021). Matrix Refinement in Mass Transport Across Fracture-Matrix Interface: Application to Improved Oil Recovery in Fractured Reservoirs. In *Abu Dhabi International Petroleum Exhibition & Conference* (p. D011S003R001). <https://doi.org/10.2118/208038-MS>
- Brown, M. (2013). Granite; from genesis to emplacement. *Geological Society of America Bulletin*, 125(7–8), 1079–1113. <https://doi.org/10.1130/B30877.1>
- Bruce Hill, L. (2021). *Superhot Rock Geothermal: A Vision for Zero-Carbon Energy “Everywhere.”* [https://www.catf.us/wp-content/uploads/2021/09/CATF\\_SuperhotRockGeothermal\\_Report.pdf](https://www.catf.us/wp-content/uploads/2021/09/CATF_SuperhotRockGeothermal_Report.pdf)
- Cho, Y. (2012). *Effects of pressure-dependent natural-fracture permeability on shale-gas well production.* Colorado School of Mines. Arthur Lakes Library. <http://hdl.handle.net/11124/16314>
- Eker, E., Uzun, I., & Kazemi, H. (2017). Numerical Simulation of Dual-Porosity Multiphase Flow Using Poroelasticity Theory. In *SPE Reservoir Simulation Conference* (p. D031S010R005). <https://doi.org/10.2118/182728-MS>
- Frost, B. R., Barnes, C. G., Collins, W., Arculus, R. J., Ellis, D. J., & Frost, C. D. (2001). A Geochemical Classification for Granitic Rocks. *Journal of Petrology*, 42(11), 2033–2048. <https://doi.org/10.1093/petrology/42.11.2033>
- Geology. (2022). *Geology | Open Energy Information. Utah FORGE Geology.* <https://openei.org/wiki/Geology>

10. Jones, S. C. (1972). A Rapid Accurate Unsteady-State Klinkenberg Permeameter. *Society of Petroleum Engineers Journal*, 12(05), 383–397. <https://doi.org/10.2118/3535-PA>
11. Kirby, S.M., Knudsen, T., Kleber, E., & Hiscock., A. (2018). Geologic setting of the Utah FORGE site, based on new and revised geologic mapping. *Trans. Geotherm. Resour. Counc*, 42, Pp.1097-1114. <https://publications.mygeoenergynow.org/grc/1034017.pdf>
12. Kumar, D., & Ghassemi, A. (2019). Multistage Hydraulic Fracturing of EGS Wells with Application to FORGE. *Proceedings, 44th Workshop on Geothermal Reservoir Engineering Stanford University, Stanford, California, February 11-13, 2019. SGP-TR-214*. <https://pangea.stanford.edu/ERE/db/GeoConf/papers/SGW/2019/Kumar.pdf>
13. Kurtoglu, B., Torcuk, M. A., & Kazemi, H. (2012). Pressure Transient Analyses of Short and Long Duration Well Tests in Unconventional Reservoirs. In *SPE Canadian Unconventional Resources Conference* (p. SPE-162473-MS). <https://doi.org/10.2118/162473-MS>
14. Medeiros, F., Kurtoglu, B., Ozkan, E., & Kazemi, H. (2007). Pressure-Transient Performances of Hydraulically Fractured Horizontal Wells in Locally and Globally Naturally Fractured Formations. In *International Petroleum Technology Conference* (p. IPTC-11781-MS). <https://doi.org/10.2523/IPTC-11781-MS>
15. Medeiros, F., Ozkan, E., & Kazemi, H. (2008). Productivity and Drainage Area of Fractured Horizontal Wells in Tight Gas Reservoirs. *SPE Reservoir Evaluation & Engineering*, 11(05), 902–911. <https://doi.org/10.2118/108110-PA>
16. Moore, J., McLennan, J., Pankow, K., Simmons, S., Podgorney, R., Wannamaker, P., Jones, C., Rickard, W., & Xing, P. (2020). The Utah Frontier Observatory for Research in Geothermal Energy (FORGE): A Laboratory for Characterizing, Creating and Sustaining Enhanced Geothermal Systems. *Proceedings, 45th Workshop on Geothermal Reservoir Engineering, Stanford University, Stanford, California, February 10-12, 2020. SGP-TR-216*.
17. Nadimi, S., Forbes, B., Moore, J., Podgorney, R., & McLennan, J. D. (2020). Utah FORGE: Hydrogeothermal modeling of a granitic based discrete fracture network. *Geothermics*, 87, 101853. <https://doi.org/https://doi.org/10.1016/j.geothermics.2020.101853>
18. Simmons, S., Kirby, S., Jones, C., Moore, J., Allis, R., Brandt, A., & Nash, G. (2016). The geology, geochemistry, and geohydrology of the FORGE deep well site, Milford, Utah. *Proceedings, 41st Workshop on Geothermal Reservoir Engineering, Stanford University, California, 10 P*.
19. Utah FORGE. (2019). *Numerical Modeling: Modeled Granitoid Parameters*. Modeling and Simulation Forum. <https://utahforge.com/laboratory/numerical-modeling/>
20. Wells, D., Lin, F.-C., Pankow, K., Baker, B., & Bartley, J. (2022). Combining Dense Seismic Arrays and Broadband Data to Image the Subsurface Velocity Structure in Geothermally Active South-Central Utah. *Journal of Geophysical Research: Solid Earth*, 127(7), e2022JB024070. <https://doi.org/https://doi.org/10.1029/2022JB024070>
21. Winkler, D., Swearingen, L., & McLennan, J. (2021). *Utah FORGE: Well 16A(78)-32: Summary of Drilling Activities*. <https://gdr.openei.org/submissions/1296>
22. Xing, P., McLennan, J., & Moore, J. (2020). In-Situ Stress Measurements at the Utah Frontier Observatory for Research in Geothermal Energy (FORGE) Site. *Energies*, 13(21). <https://doi.org/10.3390/en13215842>